

# Mo-Terminated Edge Reconstructions in Nanoporous Molybdenum Disulfide Film

Xiaoxu Zhao,<sup>†,‡,§,||,ID</sup> Deyi Fu,<sup>†,||,ID</sup> Zijing Ding,<sup>†</sup> Yu-Yang Zhang,<sup>§,⊥</sup> Dongyang Wan,<sup>#</sup> Sherman J. R. Tan,<sup>†,‡,ID</sup> Zhongxin Chen,<sup>†,‡</sup> Kai Leng,<sup>†,ID</sup> Jiadong Dan,<sup>‡,○</sup> Wei Fu,<sup>†</sup> Dechao Geng,<sup>†</sup> Peng Song,<sup>†</sup> Yonghua Du,<sup>▽,ID</sup> T. Venkatesan,<sup>‡,#,○,◆,¶</sup> Sokrates T. Pantelides,<sup>⊥</sup> Stephen J. Pennycook,<sup>‡,○</sup> Wu Zhou,<sup>\*,§,ID</sup> and Kian Ping Loh<sup>\*,†,ID</sup>

<sup>†</sup>Department of Chemistry and Centre for Advanced 2D Materials (CA2DM), National University of Singapore, 3 Science Drive 3, Singapore, 117543, Singapore

<sup>‡</sup>NUS Graduate School for Integrative Sciences and Engineering, National University of Singapore, 13 Centre for Life Sciences, #05-01, 28 Medical Drive, Singapore 117456, Singapore

<sup>§</sup>School of Physical Sciences and CAS Center for Excellence in Topological Quantum Computation, University of Chinese Academy of Sciences, Beijing 100049, China

<sup>||</sup>SinBeRISE CREATE, National Research Foundation, CREATE Tower, 1 Create Way, Singapore 138602, Singapore

<sup>⊥</sup>Department of Physics and Astronomy and Department of Electrical Engineering and Computer Science, Vanderbilt University, Nashville, Tennessee 37235, United States

<sup>#</sup>NUSNNI-NanoCore, National University of Singapore, 117411, Singapore

<sup>▽</sup>Institute of Chemical and Engineering Sciences, Agency for Science, Technology and Research, 1 Pesek Road, Jurong Island 627833, Singapore

<sup>○</sup>Department of Materials Science and Engineering, National University of Singapore, 9 Engineering Drive 1, 117575, Singapore

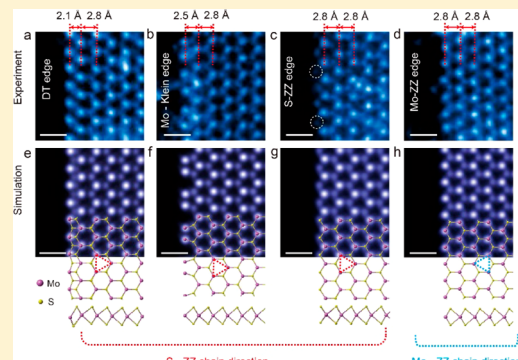
<sup>◆</sup>Department of Electrical and Computer Engineering, National University of Singapore, 9 Engineering Drive 1, 117575, Singapore

<sup>¶</sup>Department of Physics, National University of Singapore, 2 Science Drive 3, 517551, Singapore

## Supporting Information

**ABSTRACT:** The catalytic and magnetic properties of molybdenum disulfide ( $\text{MoS}_2$ ) are significantly enhanced by the presence of edge sites. One way to obtain a high density of edge sites in a two-dimensional (2D) film is by introducing porosity. However, the large-scale bottom-up synthesis of a porous 2D  $\text{MoS}_2$  film remains challenging and the correlation of growth conditions to the atomic structures of the edges is not well understood. Here, using molecular beam epitaxy, we prepare wafer-scale nanoporous  $\text{MoS}_2$  films under conditions of high Mo flux and study their catalytic and magnetic properties. Atomic-resolution electron microscopy imaging of the pores reveals two new types of reconstructed Mo-terminated edges, namely, a distorted 1T (DT) edge and the Mo-Klein edge. Nanoporous  $\text{MoS}_2$  films are magnetic up to 400 K, which is attributed to the presence of Mo-terminated edges with unpaired electrons, as confirmed by density functional theory calculation. The small hydrogen adsorption free energy at these Mo-terminated edges leads to excellent activity for the hydrogen evolution reaction.

**KEYWORDS:** *Molybdenum disulfide, edge magnetism, hydrogen evolution reactions, transition metal dichalcogenides*



2D transition metal dichalcogenides (TMDCs) have attracted tremendous interests over the past few years due to their extraordinary catalytic,<sup>1–5</sup> magnetic,<sup>6–9</sup> electrical,<sup>10</sup> and optical<sup>11,12</sup> properties. So far, much of the effort has been focused on the growth of large single crystalline TMDC monolayers<sup>13,14</sup> with the aim to fully exploit their excellent properties predicted by theory. The performance gap between theoretically predicted properties as compared to what is actually observed experimentally, has been typically attributed

to the presence of imperfections in the crystal, which lead to mesoscopic electrical inhomogeneity and topological disorder.<sup>15</sup> However, in certain applications such as catalysis, defects in the form of vacancies, pores or grain boundaries, can be helpful. In addition, the presence of unpaired electrons induced

**Received:** October 17, 2017

**Revised:** November 13, 2017

**Published:** December 18, 2017



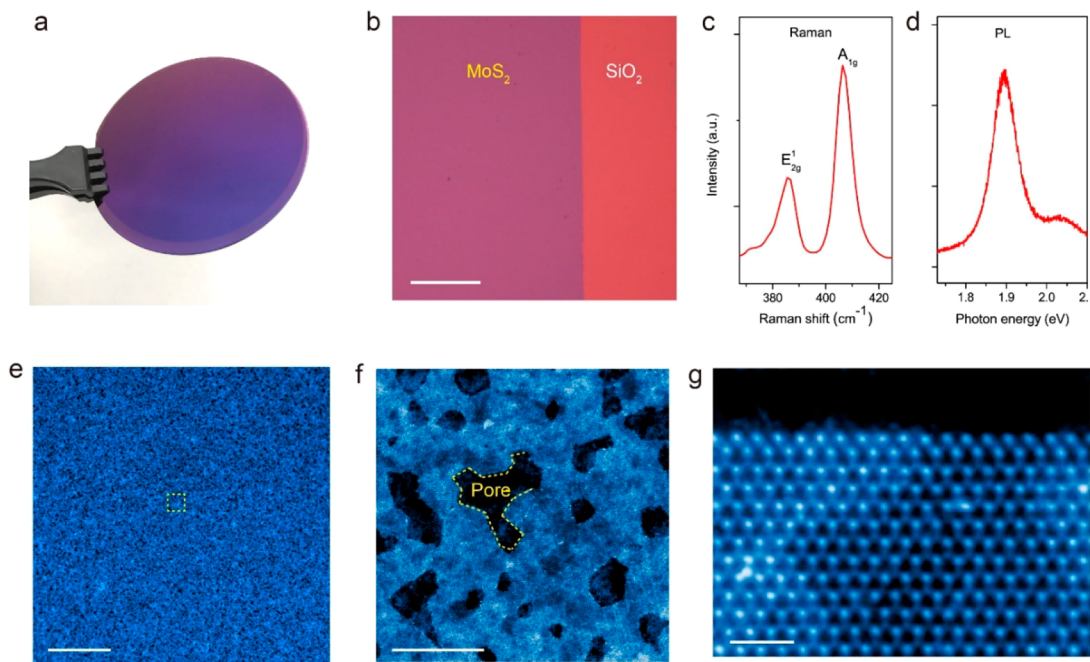


**Figure 1.** Wafer-scale homogeneous nanoporous monolayer MoS<sub>2</sub> film grown by MBE. (a) Photograph of the as-grown nanoporous MoS<sub>2</sub> film on a 2 in. SiO<sub>2</sub>/Si wafer. (b) Optical images of the edge region showing the high homogeneity. (c) Raman and (d) PL spectra of the as-grown nanoporous MoS<sub>2</sub> film. (e,f) STEM-ADF images of the nanoporous MoS<sub>2</sub> film at different field of views showing the homogeneous distribution of nanopores. (g) Atomic-resolution STEM-ADF images showing atomically sharp DT edges. The inhomogeneous contrast observed in (e–g) is induced by the transfer residues, that is, hydrocarbons and silicon oxides. Scale bars: 100 μm (b), 500 nm (e), 20 nm (f), and 1 nm (g).

by the structural discontinuity at the edges and boundaries of 2D materials presents a unique opportunity to investigate the complex interplay between the edge structure and chemical reactivity in these materials.<sup>5,6,16,17</sup> Two types of edges, namely, armchair and zigzag, are commonly observed in 2D crystals with the hexagonal phase. Experimental observations have indicated that for monolayer MoS<sub>2</sub>, the predominantly zigzag edges are oriented either along the directions of the Mo-zigzag (Mo-ZZ) chain or the S-zigzag (S-ZZ) chain depending on the chemical potential of Mo (or S), for example, partial pressure in MBE.<sup>18,19</sup> Such edge sites are particularly important for the catalytic performance of TMDCs, because the perfect basal plane is relatively inert and only the edge sites are chemically active.<sup>4–6</sup> In addition, it has been demonstrated that edge sites can induce magnetism in TMDCs.<sup>7</sup> Theoretical studies<sup>8,9</sup> suggest that basal planes remain nonmagnetic, while zigzag edges can have a magnetic ground state. Recently, it has also been shown that nonlinear sub-band transitions related to edge states can modify the optical properties of MoS<sub>2</sub>.<sup>12</sup>

To study the effect of edges on the properties of MoS<sub>2</sub>, it is necessary to create a wide spectrum of edge topologies and this can be achieved by growing a highly porous film, as pores have large numbers of different types of edge atoms, which relax differently when compared to atoms in the basal plane. Here, we report the successful growth of a wafer-scale, nanoporous monolayer MoS<sub>2</sub> film ( $\sim 22.5 \pm 0.6\%$  per total area) via molecular beam epitaxy (MBE) under conditions of high Mo flux (see Methods), with the aim of generating a high density of Mo-terminated edges. The average diameter of the as-grown pores is  $\sim 9$  nm and the total edge density is estimated to be  $1.9 \pm 0.1 \times 10^2$  m/mm<sup>2</sup>, which is  $\sim 1700$  times higher than that in conventional chemical vapor deposition (CVD)-grown MoS<sub>2</sub> monolayers (see Methods). The nanoporous MoS<sub>2</sub> film obtained exhibits a distinct magnetic moment up to 400 K and

shows a robust and significantly higher HER performance than MoS<sub>2</sub> films reported in the literature.<sup>1,2,5,20–25</sup> Scanning transmission electron microscopy–annular dark-field (STEM-ADF) imaging was employed to characterize the atomic structure of the edge sites. In addition to conventional Mo- and S-terminated zigzag edges, we have also observed two new edge structure types terminating along the S-ZZ chain direction, namely, the distorted T (DT) edge and the Mo-Klein edge, where Mo atoms are the outermost terminating atoms. Density functional theory (DFT) calculations reveal that the DT, Mo-Klein, and Mo-ZZ edges show magnetic moments of 0.50, 1.01, and 0.90 μB per Mo atom, respectively. The calculated hydrogen adsorption free energy (ΔG<sub>H</sub>) for both DT and Mo-ZZ edges are  $-0.08$  and  $0.06$  eV, which allows reversible hydrogen adsorption/desorption, thus affording high HER performances.

The MoS<sub>2</sub> films used in this study were grown on 2 inch wide, 285 nm-thick SiO<sub>2</sub>/Si wafers in a dedicated MBE setup at different temperatures and with relatively high Mo/S flux ratios (see Methods for more details). Ultrapure Mo and S molecular beams were evaporated, respectively, from an e-beam evaporator and a valved sulfur cracker cell. The as-grown MoS<sub>2</sub> film is highly homogeneous, as shown in the photograph (Figure 1a), optical images (Figure 1b), and scanning electron microscopy (SEM) images (Figure S1). Raman and photoluminescence (PL) spectroscopy (Figure 1c,d) were performed to characterize the film quality. The Raman spectrum shows two prominent peaks located at 386.2 and 406.7 cm<sup>-1</sup>, which correspond, respectively, to the in-plane E<sub>2g</sub><sup>1</sup> and out-of-plane A<sub>1g</sub> vibration modes and is comparable to that observed for MoS<sub>2</sub> monolayers prepared by mechanical exfoliation.<sup>26</sup> A strong PL peak located at  $\sim 1.88$  eV and a shoulder peak located at  $\sim 2.04$  eV is consistent with the A and B excitonic emissions.<sup>13</sup> X-ray photoelectron spectroscopy (Figure S2)

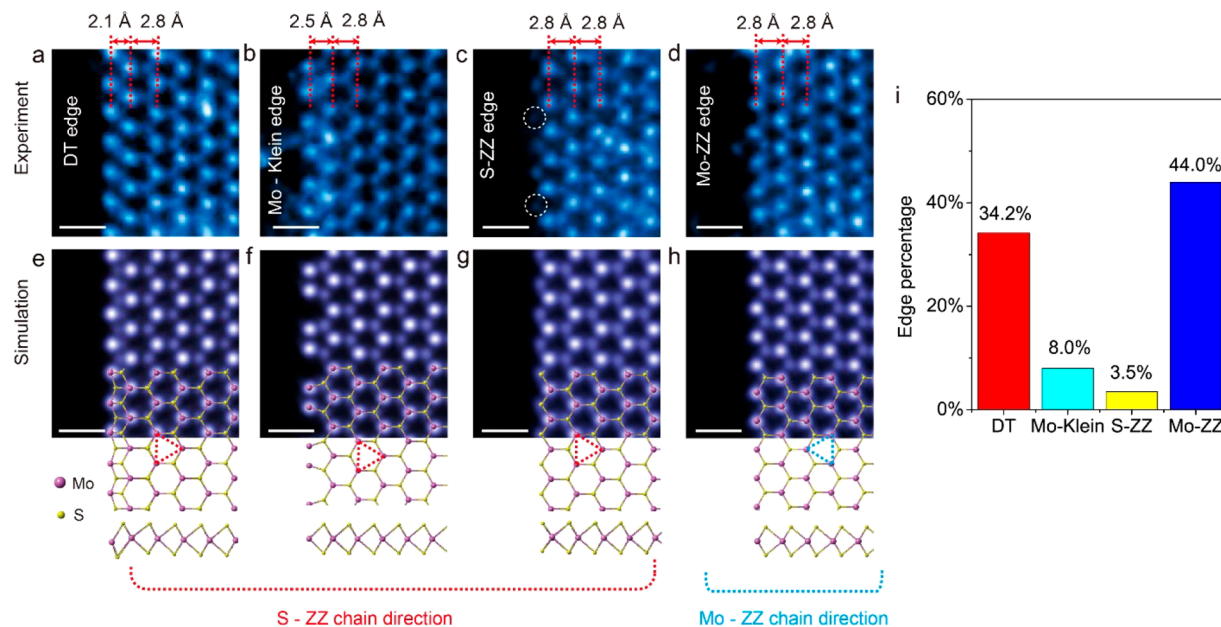


**Figure 2.** Electron microscopy study of the nanoporous MoS<sub>2</sub> film. (a–d) Atomic-resolution STEM-ADF images showing the (a) DT, (b) Mo-Klein, (c) S-ZZ, and (d) Mo-ZZ edges. (e–h) Simulated images with overlaid DFT optimized atomic structures of the (e) DT, (f) Mo-Klein, (g) S-ZZ, and (h) Mo-ZZ edges. (i) Histograms of the various edges in the nanoporous MoS<sub>2</sub> film. Scale bars: 0.5 nm.

further confirms that the film has the stoichiometric chemical composition of MoS<sub>2</sub> without detectable contamination.<sup>12,13</sup> Film thickness and homogeneity is further validated by atomic force microscopy (AFM) (Figure S1) and Raman mapping (Figure S1).

Porosity is introduced into the MoS<sub>2</sub> thin films by employing a relatively fast growth rate and low growth temperature (300 °C for 2 h); these conditions are selected to suppress the lateral diffusion of adatoms, thus producing incompletely coalesced films.<sup>27</sup> The STEM-ADF image shown in Figure 1e indicates that the as-grown film is fully decorated with nanopores, which is further supported by enlarged images as depicted in Figure 1f (dark holes highlighted by yellow dashed lines). The percentage of the pore area with respect to the total area is  $\sim 22.5 \pm 0.6\%$ , and the calculated edge density is  $\sim 1.9 \pm 0.1 \times 10^2 \text{ m/mm}^2$ , which is more than 3 orders of magnitude higher than in MoS<sub>2</sub> single crystals grown by CVD method (see Methods). The fast Fourier transform (FFT) pattern (Figure S3) in Figure 1f indicates that the as-grown MoS<sub>2</sub> film is polycrystalline and the reconstructed inverse FFT image (Figure S3) reveals the average grain size to be  $\sim 85 \text{ nm}^2$ , that is, with an average lateral size of  $\sim 9 \text{ nm}$ . It is worth noting that if the growth temperature is raised to increase the rate of adatom diffusion, a continuous film with a larger grain size and low porosity can be formed (Figure S4).

Using a MoS<sub>2</sub> nanoribbon as an example, we observe that the edges are regions of polar discontinuity; two types of stable edges are observed, namely, the Mo-ZZ edge and the S-ZZ edge, which terminate on either side of the nanoribbon.<sup>28,29</sup> Depending on the chemical potential of the constituent atoms during the growth, the Mo-ZZ edges or S-ZZ edges can be further terminated by S or Mo atoms with different types of reconstructions.<sup>18,30</sup> To investigate the topological variations of the edge sites in the as-grown nanoporous MoS<sub>2</sub> film, the atomic configurations of the edges are characterized by a combination of atomic-resolution STEM-ADF imaging and rationalized by DFT calculations. Interestingly, we observed

two new topological structures which occurred at relatively high density, which we named as the distorted 1T (DT) edge and Mo-Klein. Statistical sampling (Figure 2i) from random locations (total investigated pore perimeter is  $\sim 1720 \text{ nm}$ ) reveals that the four predominant edges Mo-ZZ, DT, Mo-Klein, and S-ZZ are distributed with population percentages of 44.0%, 34.2%, 8.0%, and 3.5%, respectively, over the entire edge length (the remaining  $\sim 10\%$  of the edge sites are irregular). Note that DT, Mo-Klein, and S-ZZ edges are all terminated along the S-ZZ chain directions.

An atom-resolved STEM-ADF image (Figure 1g and Figure 2a) of the DT edge reveals that its topological configuration is distinctly different from that of the S-ZZ edge. The outermost atoms in the DT edge are made of a strip of Mo atoms instead of a strip of sulfur dimers as in the S-ZZ edge. In addition, the coordination of the outermost Mo atoms decreases to 3-fold, whereas, it is 4-fold and 6-fold, respectively, for the outermost Mo atoms in the Mo-ZZ edge and the interior basal planes. The lowering of coordination implies a Mo-rich local stoichiometry as well as the presence of additional unpaired Mo<sub>4d</sub> electrons in the DT edge. The simulated STEM-ADF image (Figure 2e) based on a DFT optimized DT edge model (Figure 2e overlaid) resembles the experimental image at all atomic positions. It is known that MoS<sub>2</sub> monolayers adopt a wide variety of polymorphs with the well-known 1H polymorph being the most stable configuration in the natural and synthetic MoS<sub>2</sub>. The 1H polymorph consists of two layers of sulfur atoms stacked in an eclipsed configuration and the symmetry of the resulting trigonal prism configuration belongs to point group D<sub>3h</sub>. The DT edge, however, shows a distinct 1T type polymorph,<sup>31,32</sup> where two layers of sulfur atoms are in a staggered configuration forming an octahedral antiprism configuration of D<sub>3d</sub> symmetry. Theoretical studies suggest that the 1T phase is dynamically unstable<sup>12,33</sup> and undergoes a Peierls distortion; this introduces a periodic distortion of the lattice, giving rise to the so-called distorted 1T phase (1T'). The DT edge has a contracted in-plane Mo–Mo distance of

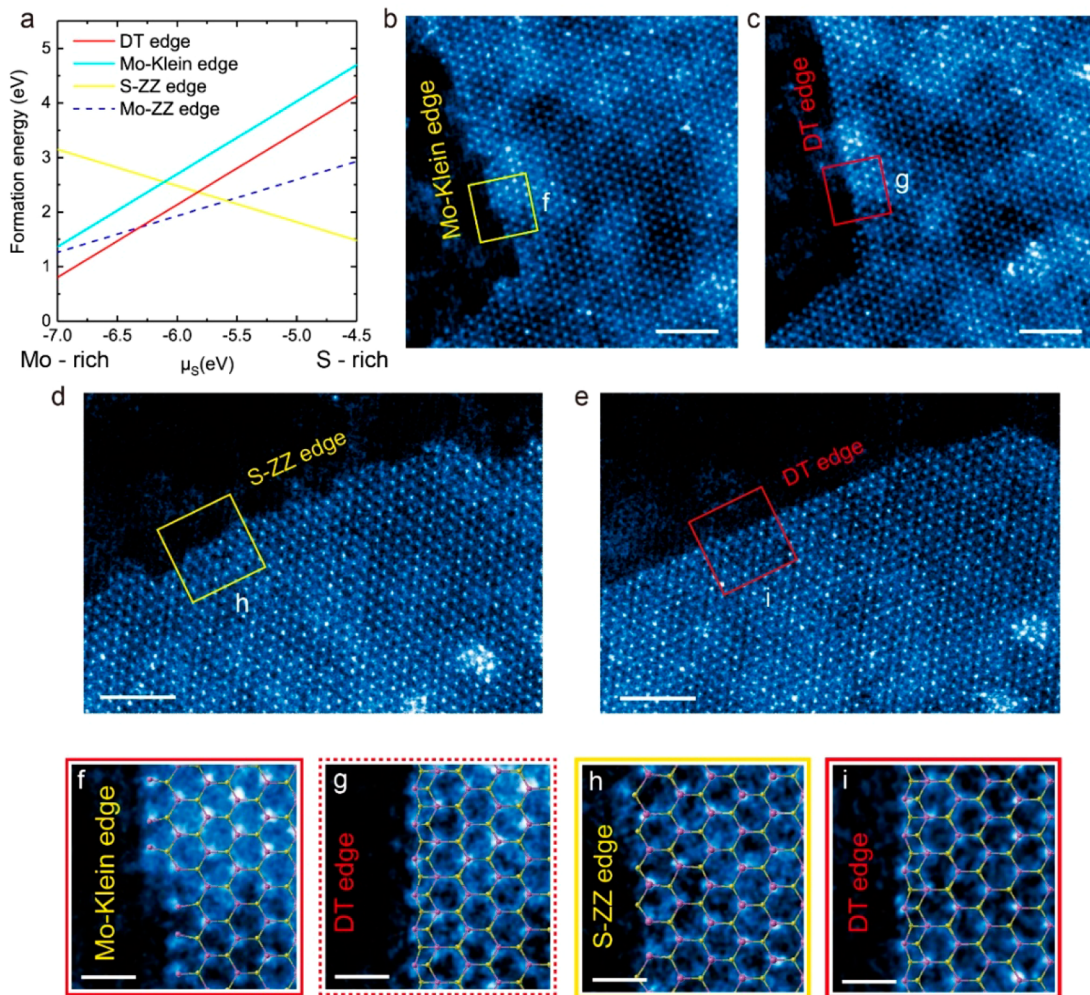


**Figure 3.** Thermodynamic stability of the various edges. (a) Calculated formation energies of the different types of edges in 2D MoS<sub>2</sub> as a function of sulfur chemical potential. STEM-ADF images of a region in the sample (b) before and (c) after in situ annealing at 900 °C for 30 min inside the microscope revealing the edge transformation from Mo-Klein edges to DT edges. In parallel, STEM-ADF images of another region in the sample (d) before and (e) after in situ annealing at 900 °C for 30 min inside the microscope showing the edge transformation from S-ZZ edges to DT edges. (f) Enlarged STEM-ADF images of the Mo-Klein edges from the region highlighted in panel b evolved into a (g) DT edge, as highlighted in the red box region in panel c. (h) Enlarged STEM-ADF images of the S-ZZ edge from the region highlighted in panel d evolved into a (i) DT edge, as highlighted in the red box region in panel e. Scale bars: 2 nm (b–e); 0.5 nm (f–i).

2.1 Å (2.7 Å in bulk region), which is similar to the projected Mo–Mo in-plane distance (2.2 Å) in 1T'-MoS<sub>2</sub> (Figure S5). It is known that 1T'-MoS<sub>2</sub> exhibits different catalytic, magnetic, and optical properties as compared to the 2H phase,<sup>17,22,31,34</sup> but the metastability of the 1T' phase hinders its use in practical applications.<sup>12</sup> Here, we discover that the DT phase can be stabilized at the edges while conserving the H phase in the basal plane. In fact, we found that the DT edge is the most thermodynamically stable configuration among the different types of edges terminating along the S-ZZ chain directions.

Another edge structure, which we named as the Mo-Klein edge (Figure 2b), was also observed. The Klein-type edge has been reported in graphene,<sup>35,36</sup> in which first-principles calculations predict interesting magnetic properties,<sup>37</sup> however, its analogues have not been reported for MoS<sub>2</sub> or other 2D materials. Here, an atom-resolved STEM-ADF image of the Mo-Klein edge is depicted in Figure 2b. As compared to the DT edge, the coordination number of the outermost Mo atom is further reduced to two, even though the chemical stoichiometry is the same for both DT and Mo-Klein edges.

Periodic Mo–Mo dimerization has been found both experimentally (Figure 2b) and theoretically (Figure 2f), leading to a unique alternating elongated/shortened metal–metal bonding network. On the other hand, the S-ZZ edge (Figure 2c) is rarely observed across the film and it accounts for only ~3.9% of the total number of edges. The S-ZZ edge is not stable under electron beam irradiation, and sulfur vacancies are occasionally observed as highlighted by white dashed circles in Figure 2c. Other possible edge-types are listed in Figure S6. The (bare) Mo-ZZ edge (Figure 2d) is the most common edge type observed (almost half of the total edges).

In order to understand the formation mechanism of these edges, the formation energies of the different edges are calculated and plotted as a function of sulfur chemical potential<sup>30</sup> as shown in Figure 3a. Among the different edge terminations (DT (red), Mo-Klein (cyan), and S-ZZ edge (yellow)) along the S-ZZ chain direction, the S-ZZ edge shows increasing formation energy with decreasing sulfur chemical potential, in contrast to the other two edges. Under the Mo-rich condition, the formation energy of the S-ZZ edge increases which renders it less energetically favored. Therefore,

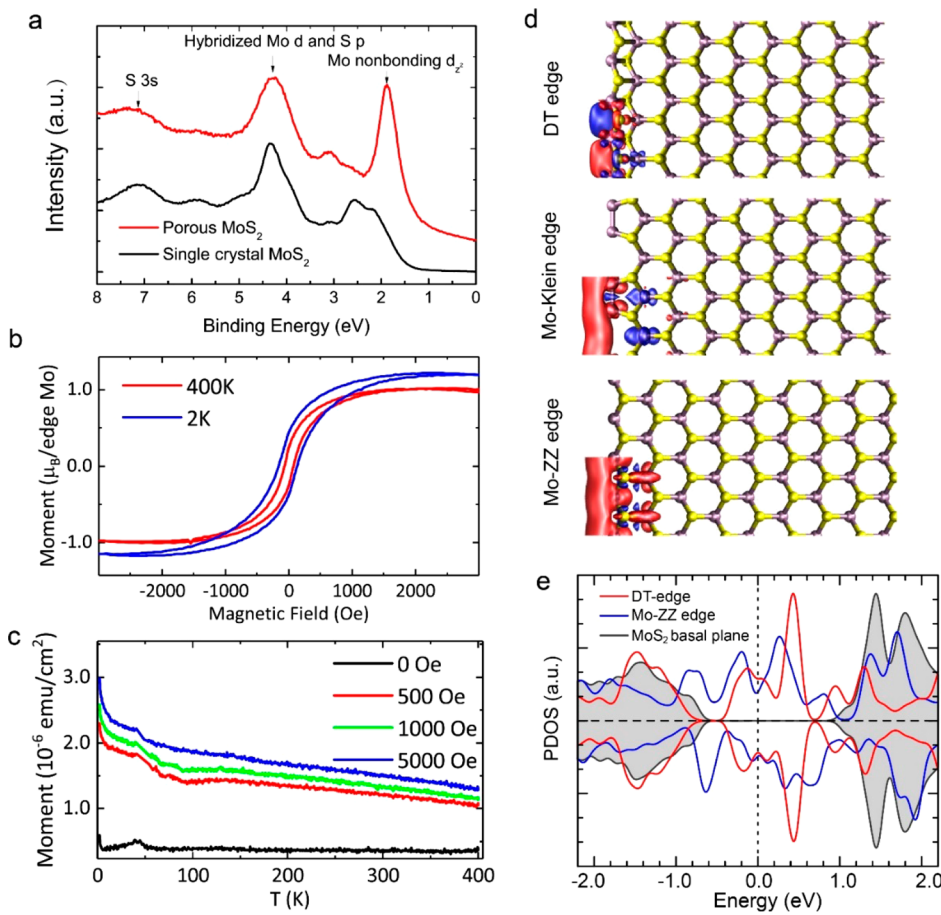


**Figure 4.** Magnetic properties of the nanoporous MoS<sub>2</sub> film. (a) Ultraviolet photoelectron spectroscopy (UPS) spectra of (red) the nanoporous MoS<sub>2</sub> film and (black) single crystal MoS<sub>2</sub> grown by CVD. (b) Magnetization vs magnetic field ( $M$ – $H$ ) curves at 2 K (blue curve) and at 400 K (red curve) of the nanoporous MoS<sub>2</sub> film. (c) Temperature dependence ( $M$ – $T$  curves) of FC and ZFC magnetization. (d) Top views of the spin density distribution at the DT, Mo-Klein, and Mo-ZZ edges. (e) Spin-polarized projected density of states (PDOS) of the (red) DT edge, (blue) Mo-ZZ edge, and (gray) interior basal plane. The Fermi level is set to zero.

it is easy to understand that the S-ZZ edge has the lowest population in our as-grown sample (Figure 2i). The DT edge appears to be the most stable topological edge structure terminating along the S-ZZ chain direction under Mo-rich conditions, which can be explained by its lower formation energy than that of the Mo-Klein edge by 0.56 eV per unit cell. In terms of the edge terminations along Mo-ZZ chain direction, the bare Mo-ZZ edge exhibits a lower formation energy than the sulfur-terminated Mo-ZZ edge (Figure S7). Hence, we can conclude that the edges (DT, Klein, and Mo-ZZ) observed in our nanoporous MoS<sub>2</sub> film are mostly Mo-terminated under Mo-rich synthesis conditions.

Next, *in situ* annealing experiments were performed in the microscope (pressure  $< 3 \times 10^{-9}$  T) to investigate the thermodynamic stability of the different types of edges. STEM-ADF images of a randomly chosen region containing predominantly S-ZZ edges, before and after annealing, are shown in Figure 3d,e. It was observed that all the S-ZZ edges (Figure 3d) transform into DT edges (Figure 3c) after annealing at 900 °C for 30 min, which is consistent with the fact that DT edges have the lowest formation energy at Mo-rich conditions (Figure 2i). The resulting DT edge is atomically sharp and smooth. In parallel, the *in situ* transformation of the Mo-Klein edge to the DT edge (Figure 3b,c) is also observed during annealing. These results clearly prove that the DT edge is the most thermodynamically stable

topological structure among the different terminations along the S-ZZ chain direction and maintains its structural integrity even at 900 °C. It is worth noting that the DT edge is also stable under ambient conditions and atomically sharp images of this edge can be observed even after exposing the sample to air for one month. In contrast to the S-ZZ edges, the Mo-ZZ edge is highly stable and remains unchanged after *in situ* annealing at 900 °C, the results are shown in Figure S8.

Ultraviolet photoelectron spectroscopy (UPS) was employed to probe the chemical environment of Mo in the nanoporous MoS<sub>2</sub> films. The UPS spectrum (Figure 4a) reveals that the density of states (DOS) of nanoporous MoS<sub>2</sub> resembles that of single-crystal MoS<sub>2</sub> grown by CVD in the energy range 3–8 eV. The valence band maximum near 2 eV is strongly enhanced due to the contribution from nonbonding Mo d<sub>z<sup>2</sup></sub> orbitals, indicating an increased proportion of under-coordinated Mo atoms in the nanoporous MoS<sub>2</sub> film.<sup>38</sup>

In a nanoporous MoS<sub>2</sub> film, the presence of Mo atoms with low coordination numbers gives rise to unpaired Mo<sub>4d</sub> electrons.<sup>8,9,17,18</sup> To investigate if the spins of these unpaired electrons can be aligned by a magnetic field, magnetization versus applied magnetic field ( $M$ – $H$ ) curves were measured using a superconducting quantum interface device (SQUID) magnetometer. The magnetic measurement was carried out immediately after the sample growth to avoid any external contamination. As seen in Figure 4b, well-defined magnet-

ization hysteresis loops are obtained at 2 and 400 K, confirming a robust magnetic moment at temperatures well above room temperature. The remanence ( $M_R$ ) and saturation magnetization ( $M_S$ ) at 2 K is calculated to be  $0.5 \mu\text{B}$  and  $1.1 \mu\text{B}$  per Mo edge atom (see *Methods*), respectively. A clear divergence is observed with change in temperature ( $M-T$  curves, *Figure 4c*) as shown in zero-field-cooling (ZFC) and field-cooling (FC) curves, and the Curie temperature ( $T_c$ ) is believed to be much higher than 400 K since no sign of any change in magnetic properties is observed.

To understand the origin of the magnetic moment, we have calculated the spatially resolved spin density in the three predominant edge types as shown in *Figure 4d* and *Figure S9*, where the local spin-up and spin-down electron densities are highlighted by red and blue false color, respectively. Notably, in all types of edges, the magnetic states originate mainly from the Mo atoms at the edges, thus confining the magnetic moment to the edge regions. Interestingly, Mo atoms along the DT edge show periodically alternating spin directions, with opposing spins having almost the same magnitude. Thus, the internal magnetic structure is antiferromagnetic. In contrast, both Mo-Klein and Mo-ZZ edges reveal ferromagnetic characteristics. Theoretical calculations further indicate that the Mo-ZZ edge, Mo-Klein edge, and DT edge exhibit magnetic moments of, respectively,  $0.90 \mu\text{B}$ ,  $1.01 \mu\text{B}$ , and  $0.50 \mu\text{B}$  per Mo edge atom. These values are comparable in magnitude to our experimental observation. We are aware that atomic defects,<sup>39</sup> line defects,<sup>40</sup> and grain boundaries<sup>41</sup> can also contribute additional magnetic moments to the nanoporous MoS<sub>2</sub> film. To evaluate the importance of these contributions from structural defects, a continuous MoS<sub>2</sub> film containing a comparable density of structural defects (vacancies, grain boundaries, etc.), but without porosity, was tested (*Figure S10*). We found that the  $M_S$  of such a continuous, defective MoS<sub>2</sub> film is about one-fourth of the nanoporous MoS<sub>2</sub> film, thereby confirming that the edge sites have major contributions to the magnetic moment in the nanoporous MoS<sub>2</sub> film.

Spin-polarized projected density of states (PDOS) mapping of the edge regions allows us to examine the spectral distribution of the spin directions (up and down spins) in the different types of edges. *Figure 4e* shows the spin-polarized LDOS of a MoS<sub>2</sub> nanoribbon terminated by Mo-ZZ and DT edges. The MoS<sub>2</sub> basal plane (gray curve) shows a bandgap of 1.8 eV, whereas the DT edge (red curve), the Mo-ZZ edge (blue curve), and the Mo-Klein edge (*Figure S11*) are all metallic. Significantly, the projected PDOS for spin-up and spin-down states in the DT edge have almost the same spectral density, which leads to antiferromagnetism in the DT edge. On the other hand, the spin-polarized PDOS of spin-up and spin-down states in the Mo-ZZ edge (blue curve) and the Mo-Klein edge (*Figure S11*) clearly demonstrate ferromagnetic behaviors.

According to our PDOS calculations, the edges in nanoporous MoS<sub>2</sub> films are metallic and contain nonbonding Mo<sub>4d</sub> electrons, suggesting that this material can be a good catalyst. Prompted by this, we tested the nanoporous film for the hydrogen evolution reaction (HER). From the linear sweep voltammograms (LSV, *Figure S12a*), it is seen that the nanoporous MoS<sub>2</sub> film shows a substantial reduction of the onset overpotential (120 meV at  $5 \text{ mA cm}^{-2}$ ) compared to CVD-grown monolayer MoS<sub>2</sub> crystals (430 meV at  $5 \text{ mA cm}^{-2}$ ) and other nanostructured MoS<sub>2</sub> (*Figure S12d*). Nanoporous MoS<sub>2</sub> film also exhibits a significantly lower

Tafel slope (*Figure S12b*,  $54 \text{ mV dec}^{-1}$ ). Moreover, electrodes made from as-grown nanoporous MoS<sub>2</sub> films show excellent cycling stability in HER (no significant decay was observed even after 3000 cycles). These HER performance indicators are among the best values reported so far for nanostructured MoS<sub>2</sub> (*Figure S12d*). While contributions to HER activity from point defects<sup>5,42</sup> and grain boundaries<sup>42</sup> should be taken into account, these structural defects are commonly present also in CVD-, MBE-, or even in mechanically exfoliated (ME)-MoS<sub>2</sub> films,<sup>43</sup> but they do not show the same level of performance as our nanoporous MoS<sub>2</sub> film. Moreover, theoretical calculations suggest that grain boundaries<sup>42</sup> may be relatively inert for HER. Therefore, the excellent HER performance of our nanoporous MoS<sub>2</sub> is attributed mainly to the presence of abundant edge sites rather than structural defects.

HER activities of the different edges are investigated by calculating the hydrogen adsorption Gibbs free energy ( $\Delta G_H$ ), a good indicator of the HER performance of materials.<sup>44</sup> In acid conditions, the optimal value of  $\Delta G_H$  is  $\cong 0$  where the adsorption and desorption of H\* has low energy barriers. According to our calculations (see *Methods*) as shown in *Figure S12e*, the DT edge has a near-zero  $\Delta G_H$  value ( $-0.08 \text{ eV}$ ), comparable to the value for a Mo-ZZ edge ( $+0.06 \text{ eV}$ ); the latter has been found to be the most optimal site for HER in previous work.<sup>45,46</sup> Since statistical analysis of edge site population based on STEM imaging reveals that in nanoporous MoS<sub>2</sub> films, Mo-ZZ edge sites, and DT edge sites constitute  $\sim 80\%$  of all the edge sites, it can be inferred that a majority of the edge sites are catalytically active. Hence, both experimental and theoretical results validate that a nanoporous MoS<sub>2</sub> film is a good catalyst material for HER.

In conclusion, we have successfully grown wafer-scale, nanoporous MoS<sub>2</sub> monolayer films with ultrahigh edge density using MBE. Such nanoporous films allow 1D edge structures to be integrated onto a 2D platform. STEM-ADF imaging, supported by DFT calculations, reveals that the nanoporous MoS<sub>2</sub> films grown under conditions of high Mo chemical potential contain large numbers of Mo-terminated edges, for example, DT edge, Mo-Klein edge, and Mo-ZZ edge. The DT edge can be viewed as the 1D analogue of the 1T' phase, confined to the edges of the 2H-MoS<sub>2</sub> sheets. The nanoporous film also exhibits robust magnetism above room temperature and outstanding HER performance. The improved catalytic properties of nanoporous MoS<sub>2</sub> films are attributed to the presence of Mo terminated edges, for example, Mo-ZZ edges and DT edges, both of which have near-zero hydrogen absorption free energy ( $\Delta G_H$ ). Our growth strategy for nanoporous 2D MoS<sub>2</sub> films should be applicable to a wide range of TMDCs and provide a unique opportunity to study the topologies of various types of edges as well as their properties.

**Methods.** *MoS<sub>2</sub> Film Growth.* A 2 in. 285 nm-thick SiO<sub>2</sub>/Si wafer was used as the growth substrate. The MoS<sub>2</sub> film was grown in a customized MBE system with a base pressure of  $< 3 \times 10^{-10} \text{ Torr}$ . Ultrapure Mo (99.995%, Goodfellow) and S (99.5% Alfa Aesar) were evaporated, respectively, from a mini electron-beam evaporator and a valved sulfur cracker cell. The flux density of Mo was precisely controlled by setting the flux current. The output power was autoregulated to maintain a steady evaporation rate during growth. The sulfur cracker cell temperature was set to 110 °C, and the sulfur evaporation was adjusted by controlling the shutter of the cracker valve. By

adjusting the substrate temperature, the growth of a nanoporous film or a continuous highly crystalline film could be selectively controlled. A nanoporous film was grown at 300 °C for 2 h, and a continuous highly crystalline film was grown at 900 °C for 3 h. The estimated flux ratio of Mo/S is ~1:3. After growth, the Mo and S sources were turned off and the sample was annealed *in situ* for 30 min before cooling down to room temperature at a cooling rate of ~10 °C/mins. Reference MoS<sub>2</sub> crystals were grown by CVD method. The detailed method can be seen in ref 14.

**Sample Characterization.** XPS was performed using SPECS XR 50 X-ray Al K $\alpha$  (1486.6 eV) source with a pass energy of 30 eV. UPS measurements were carried out with a differentially pumped UVS300 helium discharge lamp (SPECS GmbH) as the light source, which provided a monochromatic photon energy of 21.2 eV (He I) through a toroidal mirror monochromator (SPECS GmbH). The detector used was the same as for XPS and the experiments were performed in a chamber with a base pressure lower than  $8 \times 10^{-10}$  mbar.

**STEM Sample Preparation, Characterization, and Image Simulation.** The as-grown MoS<sub>2</sub> films were transferred onto copper TEM quanti-foil grids via a conventional PMMA method. Atomic-resolution STEM-ADF imaging was carried out in an aberration-corrected Nion UltraSTEM-100, equipped with a cold field emission gun, operating at 60 kV. In situ experiments were conducted on the MEMS-based heating chip in the Nion UltraSTEM-100. STEM-ADF images with large fields of views were captured using aberration-corrected JEOL ARM200F, equipped with a cold field emission gun, operating at 60 kV. STEM-ADF image simulations were done by QSTEM with a probe size of 1 Å.

**Edge Density Calculation.** To quantitatively calculate the pore region and edge density precisely, Python scripts were employed to massively process the obtained STEM-ADF images.

**Mathematical Calculation Method.** Pore areas were determined by a threshold based on Otsu's method.<sup>47</sup> Images after segmentation was applied by a Sobel filter with proper mask size to obtain edges of pore areas. Values of pore areas were directly calculated from segmented STEM-ADF images. Edge lengths were calculated by approximating edge contours as lines through the centers of detected edge pixels using a 4-connectivity. An example is given in the Supporting Information.

**DFT Calculations.** First-principles calculations were performed based on density functional theory (DFT), employing Projector augmented-wave pseudopotentials<sup>48</sup> and the Perdew–Burke–Ernzerhof<sup>49</sup> form of the exchange-correlation functional, as implemented in the Vienna ab initio simulation package code.<sup>50</sup> The experimental MoS<sub>2</sub> lattice constant of 3.19 Å was used. We employed an energy cutoff of 280 eV for plane waves and the criterion for total energy convergence was set to  $10^{-4}$  eV. All atoms were relaxed during geometry optimization until the magnitudes of the forces were less than 0.04 eV/Å. Magnetism calculation of various edges was based on bipolar nanoribbon models shown in Figure S13. The hydrogen adsorption Gibbs free energy  $\Delta G_H$  is defined as  $\Delta G_H = \Delta E_H + \Delta E_{ZPE} - T\Delta S_H$ , where  $\Delta E_H$  is the hydrogen adsorption energy,  $\Delta E_{ZPE}$  is the difference between the zero-point energy of hydrogen adsorbed state and the gas phase H<sub>2</sub>,  $T$  is the temperature, and  $\Delta S$  is the entropy difference between hydrogen adsorbed state and the gas phase. In standard condition,  $\Delta E_{ZPE} - T\Delta S_H$  is approximately 0.25 eV.<sup>44</sup> Thus,

we use  $\Delta G_H = \Delta E_H + 0.25$  to estimate the performance of different edges.

**Magnetic and HER Property Measurements. Magnetic Moment Measurements.** The magnetization of MoS<sub>2</sub> as a function of the magnetic field ( $M-H$ ) and temperature (400 to 2 K) ( $M-T$ ) was measured in a superconducting quantum interface device (SQUID, Quantum Design). For all  $M-H$  and  $M-T$  curves, the out-of-plane magnetic moment was measured. The magnetic moment per edge Mo is calculated based on normalization of the total magnetic moment over calculated edge density.

**HER Sample Preparation and Measurement.** The as-grown MoS<sub>2</sub> film was transferred onto a 3 mm diameter glassy carbon (GC) electrode using a standard PMMA wet transfer technique. The GC plate was prepolished sequentially by 3, 1, and 0.25 μm diamond slurries. All electrochemical measurements were made under ambient conditions using a three-electrode cell. Standard Ag/AgCl electrodes and a Pt foil were used as the reference and counter electrode, respectively. Linear sweep voltammetry (LSV) was recorded in 0.5 M H<sub>2</sub>SO<sub>4</sub> electrolyte with a scan rate of 2 mV s<sup>-1</sup> on an Autolab 302 N electrochemical workstation. Tafel gradient was calculated based on at least 5 LSV curves. All potentials were calibrated with respect to a reversible hydrogen electrode.

## ■ ASSOCIATED CONTENT

### Supporting Information

The Supporting Information is available free of charge on the ACS Publications website at DOI: [10.1021/acs.nanolett.7b04426](https://doi.org/10.1021/acs.nanolett.7b04426).

Description of the methods for calculation of edge density, hydrogen evolution reaction, and supplementary figures (PDF)

## ■ AUTHOR INFORMATION

### Corresponding Authors

\*E-mail: [wuzhou@ucas.ac.cn](mailto:wuzhou@ucas.ac.cn).

\*E-mail: [chmlohkp@nus.edu.sg](mailto:chmlohkp@nus.edu.sg).

### ORCID

Xiaoxu Zhao: [0000-0001-9746-3770](https://orcid.org/0000-0001-9746-3770)

Deyi Fu: [0000-0003-1365-8963](https://orcid.org/0000-0003-1365-8963)

Sherman J. R. Tan: [0000-0003-1591-3497](https://orcid.org/0000-0003-1591-3497)

Kai Leng: [0000-0003-3408-5033](https://orcid.org/0000-0003-3408-5033)

Yonghua Du: [0000-0003-2655-045X](https://orcid.org/0000-0003-2655-045X)

Wu Zhou: [0000-0002-6803-1095](https://orcid.org/0000-0002-6803-1095)

Kian Ping Loh: [0000-0002-1491-743X](https://orcid.org/0000-0002-1491-743X)

### Author Contributions

W.Z., and K.P.L. conceived this project. W.Z. and K.P.L. supervised the execution of the whole work. X.Z. and D.F. carried out most of the experiments. X.Z. did the electron microscopy characterization and image analysis under the supervision of W.Z. and S.J.P. D.F. carried out the sample growth and basic characterizations. Z.D. calculated structures and magnetic properties of nanoribbons. Y.Y.Z and S.T.P. calculated HER activities. D.W. carried out the magnetic moment measurement under the supervision of T.V. X.Z. and Z.C. contributed to the hydrogen evolution measurement. T.J.S. did the UPS. X.Z. and T.J.S. did the XPS characterization. J.D. developed the python script. All the authors discussed the results and participated in writing the manuscript. The authors thank Dr. Jianyi Chen for providing the

CVD grown MoS<sub>2</sub> samples, and Dr. William Wai Leung Yim for helpful DFT discussions. X.Z and D.F contributed equally to this work.

## Notes

The authors declare no competing financial interest.

## ACKNOWLEDGMENTS

K.P.L thanks MOE Tier 2 grant “Porous, Conjugated Molecular Framework for Energy Storage (MOE2016-T2-1-003) and also funding by SinBeRISE CREATE, National Research Foundation, Prime Minister’s Office. W.Z. acknowledges support from the CAS Pioneer Hundred Talents Program and the Natural Science Foundation of China (51622211). Work at Vanderbilt (Y.Y.Z. and S.T.P.) was supported by the U.S. Department of Energy Grant DE-FG02-09ER46554 and by the McMinn Endowment. Computations by Y.Y.Z and S.T.P were carried out at the National Energy Research Scientific Computing Center, a DOE Office of Science User Facility supported by the Office of Science of the U.S. Department of Energy under Contract No. DE-AC02-05CH11231. The electron microscopy work was also supported through a user project at Oak Ridge National Laboratory’s Center for Nanophase Materials Sciences (CNMS), which is a DOE Office of Science User Facility. The authors thank Dr. Jianyi Chen for providing the CVD grown MoS<sub>2</sub> sample, and Dr. William Wai Leung Yim for helpful DFT discussion. S.J.P. thanks the National University of Singapore for support.

## REFERENCES

- (1) Kibsgaard, J.; Chen, Z. B.; Reinecke, B. N.; Jaramillo, T. F. *Nat. Mater.* **2012**, *11*, 963–969.
- (2) Ye, G. L.; Gong, Y. J.; Lin, J. H.; Li, B.; He, Y. M.; Pantelides, S. T.; Zhou, W.; Vajtai, R.; Ajayan, P. M. *Nano Lett.* **2016**, *16*, 1097–1103.
- (3) Hinnemann, B.; Moses, P. G.; Bonde, J.; Jorgensen, K. P.; Nielsen, J. H.; Horch, S.; Chorkendorff, I.; Norskov, J. K. *J. Am. Chem. Soc.* **2005**, *127*, 5308–5309.
- (4) Fan, X.-L.; Yang, Y.; Xiao, P.; Lau, W.-M. *J. Mater. Chem. A* **2014**, *2*, 20545–20551.
- (5) Li, H.; Tsai, C.; Koh, A. L.; Cai, L. L.; Contryman, A. W.; Fragapane, A. H.; Zhao, J. H.; Han, H. S.; Manoharan, H. C.; Abild-Pedersen, F.; Norskov, J. K.; Zheng, X. L. *Nat. Mater.* **2016**, *15*, 364.
- (6) Li, G.; Zhang, D.; Qiao, Q.; Yu, Y.; Peterson, D.; Zafar, A.; Kumar, R.; Curtarolo, S.; Hunte, F.; Shannon, S.; Zhu, Y.; Yang, W.; Cao, L. *J. Am. Chem. Soc.* **2016**, *138*, 16632–16638.
- (7) Tongay, S.; Varroosfaderani, S. S.; Appleton, B. R.; Wu, J.; Hebard, A. F. *Appl. Phys. Lett.* **2012**, *101*, 123105.
- (8) Vojvodic, A.; Hinnemann, B.; Norskov, J. K. *Phys. Rev. B: Condens. Matter Mater. Phys.* **2009**, *80*, 125416.
- (9) Peng, L.; Yao, K.; Wu, R.; Wang, S.; Zhu, S.; Ni, Y.; Zu, F.; Liu, Z.; Guo, B. *Phys. Chem. Chem. Phys.* **2015**, *17*, 10074–9.
- (10) Radisavljevic, B.; Radenovic, A.; Brivio, J.; Giacometti, V.; Kis, A. *Nat. Nanotechnol.* **2011**, *6*, 147–50.
- (11) Yin, Z.; Li, H.; Li, H.; Jiang, L.; Shi, Y.; Sun, Y.; Lu, G.; Zhang, Q.; Chen, X.; Zhang, H. *ACS Nano* **2012**, *6*, 74–80.
- (12) Tan, S. J. R.; Abdelwahab, I.; Ding, Z.; Zhao, X.; Yang, T.; Loke, G. Z. J.; Lin, H.; Verzhbitskiy, I.; Poh, S. M.; Xu, H.; Nai, C. T.; Zhou, W.; Eda, G.; Jia, B.; Loh, K. P. *J. Am. Chem. Soc.* **2017**, *139*, 2504–2511.
- (13) Chen, J.; Tang, W.; Tian, B.; Liu, B.; Zhao, X.; Liu, Y.; Ren, T.; Liu, W.; Geng, D.; Jeong, H. Y.; Shin, H. S.; Zhou, W.; Loh, K. P. *Adv. Sci.* **2016**, *3*, 1500033.
- (14) Chen, J.; Zhao, X.; Tan, S. J. R.; Xu, H.; Wu, B.; Liu, B.; Fu, D.; Fu, W.; Geng, D.; Liu, Y.; Liu, W.; Tang, W.; Li, L.; Zhou, W.; Sum, T. C.; Loh, K. P. *J. Am. Chem. Soc.* **2017**, *139*, 1073–1076.
- (15) Najmaei, S.; Amani, M.; Chin, M. L.; Liu, Z.; Birdwell, A. G.; O’Regan, T. P.; Ajayan, P. M.; Dubey, M.; Lou, J. *ACS Nano* **2014**, *8*, 7930–7.
- (16) Mathew, S.; Gopinadhan, K.; Chan, T. K.; Yu, X. J.; Zhan, D.; Cao, L.; Rusydi, A.; Breese, M. B. H.; Dhar, S.; Shen, Z. X.; Venkatesan, T.; Thong, J. T. L. *Appl. Phys. Lett.* **2012**, *101*, 102103.
- (17) Cai, L.; He, J.; Liu, Q.; Yao, T.; Chen, L.; Yan, W.; Hu, F.; Jiang, Y.; Zhao, Y.; Hu, T.; Sun, Z.; Wei, S. *J. Am. Chem. Soc.* **2015**, *137*, 2622–7.
- (18) Cao, D.; Shen, T.; Liang, P.; Chen, X.; Shu, H. *J. Phys. Chem. C* **2015**, *119*, 4294–4301.
- (19) Zhou, W.; Zou, X.; Najmaei, S.; Liu, Z.; Shi, Y.; Kong, J.; Lou, J.; Ajayan, P. M.; Yakobson, B. I.; Idrobo, J. C. *Nano Lett.* **2013**, *13*, 2615–22.
- (20) Kong, D. S.; Wang, H. T.; Cha, J. J.; Pasta, M.; Koski, K. J.; Yao, J.; Cui, Y. *Nano Lett.* **2013**, *13*, 1341–1347.
- (21) Yang, L.; Fu, Q.; Wang, W.; Huang, J.; Huang, J.; Zhang, J.; Xiang, B. *Nanoscale* **2015**, *7*, 10490–7.
- (22) Yin, Y.; Han, J. C.; Zhang, Y. M.; Zhang, X. H.; Xu, P.; Yuan, Q.; Samad, L.; Wang, X. J.; Wang, Y.; Zhang, Z. H.; Zhang, P.; Cao, X. Z.; Song, B.; Jin, S. *J. Am. Chem. Soc.* **2016**, *138*, 7965–7972.
- (23) Yu, Y. F.; Huang, S. Y.; Li, Y. P.; Steinmann, S. N.; Yang, W. T.; Cao, L. Y. *Nano Lett.* **2014**, *14*, 553–558.
- (24) Tsai, C.; Li, H.; Park, S.; Park, J.; Han, H. S.; Norskov, J. K.; Zheng, X. L.; Abild-Pedersen, F. *Nat. Commun.* **2017**, *8*, 15113.
- (25) Xie, J. F.; Qu, H. C.; Xin, J. P.; Zhang, X. X.; Cui, G. W.; Zhang, X. D.; Bao, J.; Tang, B.; Xie, Y. *Nano Res.* **2017**, *10*, 1178–1188.
- (26) Li, H.; Zhang, Q.; Yap, C. C. R.; Tay, B. K.; Edwin, T. H. T.; Olivier, A.; Baillargeat, D. *Adv. Funct. Mater.* **2012**, *22*, 1385–1390.
- (27) Tersoff, J.; Denier van der Gon, A. W. D.; Tromp, R. M. *Phys. Rev. Lett.* **1994**, *72*, 266–269.
- (28) Xu, H.; Liu, S. L.; Ding, Z. J.; Tan, S. J. R.; Yam, K. M.; Bao, Y.; Nai, C. T.; Ng, M. F.; Lu, J.; Zhang, C.; Loh, K. P. *Nat. Commun.* **2016**, *7*, 12904.
- (29) Cheng, F.; Xu, H.; Xu, W. T.; Zhou, P. J.; Martin, J.; Loh, K. P. *Nano Lett.* **2017**, *17*, 1116–1120.
- (30) Zhu, S.; Wang, Q. *AIP Adv.* **2015**, *5*, 107105.
- (31) Kappera, R.; Voiry, D.; Yalcin, S. E.; Branch, B.; Gupta, G.; Mohite, A. D.; Chhowalla, M. *Nat. Mater.* **2014**, *13*, 1128–34.
- (32) Calandra, M. *Phys. Rev. B: Condens. Matter Mater. Phys.* **2013**, *88*, 245428.
- (33) Leng, K.; Chen, Z.; Zhao, X.; Tang, W.; Tian, B.; Nai, C. T.; Zhou, W.; Loh, K. P. *ACS Nano* **2016**, *10*, 9208.
- (34) Shirodkar, S. N.; Waghmare, U. V. *Phys. Rev. Lett.* **2014**, *112*, 157601.
- (35) He, K.; Robertson, A. W.; Lee, S.; Yoon, E.; Lee, G. D.; Warner, J. H. *ACS Nano* **2014**, *8*, 12272–9.
- (36) He, K.; Robertson, A. W.; Fan, Y.; Allen, C. S.; Lin, Y. C.; Suenaga, K.; Kirkland, A. I.; Warner, J. H. *ACS Nano* **2015**, *9*, 4786–95.
- (37) Bao, Z.-q.; Shi, J.-j.; Zhang, M. *J. Appl. Phys.* **2013**, *113*, 194302.
- (38) Liang, K. S.; Hughes, G. J.; Chianelli, R. R. *J. Vac. Sci. Technol., A* **1984**, *2*, 991–994.
- (39) Komsa, H. P.; Krasheninnikov, A. V. *Phys. Rev. B* **2015**.
- (40) Li, X. M.; Long, M. Q.; Cui, L. L.; Yang, K. W.; Zhang, D.; Ding, J. F.; Xu, H. *AIP Adv.* **2016**, *6*, 015015.
- (41) Zhang, Z.; Zou, X.; Crespi, V. H.; Yakobson, B. I. *ACS Nano* **2013**, *7*, 10475–81.
- (42) Ouyang, Y. X.; Ling, C. Y.; Chen, Q.; Wang, Z. L.; Shi, L.; Wang, J. L. *Chem. Mater.* **2016**, *28*, 4390–4396.
- (43) Hong, J. H.; Hu, Z. X.; Probert, M.; Li, K.; Lv, D. H.; Yang, X. N.; Gu, L.; Mao, N. N.; Feng, Q. L.; Xie, L. M.; Zhang, J.; Wu, D. Z.; Zhang, Z. Y.; Jin, C. H.; Ji, W.; Zhang, X. X.; Yuan, J.; Zhang, Z. *Nat. Commun.* **2015**, *6*, 6293.
- (44) Tang, Q.; Jiang, D. E. *ACS Catal.* **2016**, *6*, 4953–4961.
- (45) Jaramillo, T. F.; Jorgensen, K. P.; Bonde, J.; Nielsen, J. H.; Horch, S.; Chorkendorff, I. *Science* **2007**, *317*, 100–102.

- (46) Lauritsen, J. V.; Kibsgaard, J.; Helveg, S.; Topsoe, H.; Clausen, B. S.; Laegsgaard, E.; Besenbacher, F. *Nat. Nanotechnol.* **2007**, *2*, 53–8.
- (47) Otsu, N. *IEEE Trans. Syst. Man, Cybern.* **1979**, *9*, 62–66.
- (48) Blochl, P. E. *Phys. Rev. B: Condens. Matter Mater. Phys.* **1994**, *50*, 17953–17979.
- (49) Perdew, J. P.; Burke, K.; Ernzerhof, M. *Phys. Rev. Lett.* **1996**, *77*, 3865–3868.
- (50) Kresse, G.; Hafner, J. *Phys. Rev. B: Condens. Matter Mater. Phys.* **1993**, *47*, 558–561.